https://doi.org/10.5194/wes-2026-49
Preprint. Discussion started: 31 March 2026

WIND ENERGY SCIENCE DISCUSSIONS
Open Access

Wind farm blockage in convective boundary layers

Olivier Ndindayino and Johan Meyers
Department of Mechanical Engineering, KU Leuven, Celestmnnenlaan 300, B3001 Leuven, Belgium
Correspondence: Olivier Ndindayino (olivier.ndindayino@kuleuven.be)

Abstract. This study investigates hydrostatic blockage and excitation of gravity waves in large offshore wind farms within convective boundary layers (CBLs), a regime currently underexplored compared to stable and neutral conditions. Using large-eddy simulations, the performance of a 1.5 GW wind farm is analysed across eight scenarios representative of cold-air outbreaks. These cases vary in capping-inversion height ($H = \{480, 980\}$ m) and surface temperature difference ($\Delta\theta = \{0, 3, 6, 9\}$ K), producing various convective structures, including rolls and cells. The results demonstrate that intensified convective mixing and boundary layer growth, driven by higher $\Delta\theta$, significantly alter flow physics. Enhanced buoyancy-driven turbulence improves wake recovery, leading to more uniform power distribution. Simultaneously, the growth of the boundary layer slightly reduces the magnitude of both unfavourable and favourable pressure gradients, an effect particularly pronounced in shallow boundary layers. Efficiency analysis reveals that while wake efficiency (η_{w}) increases with convective intensity, whereas non-local efficiency (η_{nl}) remains largely unaffected. Consequently, overall farm efficiency (η_{f}) improves under stronger convective forcing, though sensitivity diminishes at higher $\Delta\theta$. Despite increased mixing, hydrostatic blockage and gravity waves persist; even in deep boundary layers, a non-local efficiency of approximately 90% was recorded. Decreasing the boundary layer height, amplifies the influence of both unfavourable and favourable pressure gradients on wind farm efficiency, whereas the relative contribution of convective mixing becomes less significant.

1 Introduction

Recent studies have shown that the increasing size of offshore wind farms leads to stronger interactions with mesoscale processes (e.g., gravity waves, blockage) and highlights the importance of thermal stratification in wind farm performance. High-fidelity numerical simulations have enabled the investigation of large semi-infinite and finite wind farms in both stable boundary layers (SBLs) (Allaerts and Meyers, 2018) and conventional neutral boundary layers (CNBLs) (Allaerts and Meyers, 2017; Maas, 2023b, a; Stipa et al., 2024; Lanzilao and Meyers, 2024; Delvaux and Meyers, 2025). Their studies observed a strong adverse pressure gradient upstream (Δp_u) and a favourable pressure gradient across the farm (Δp_f), due to hydrostatic blockage and related excitation of gravity waves. Allaerts and Meyers (2018) introduced two efficiency metrics comprising the non-local efficiency $\eta_{\mathrm{nl}} = P_1/P_\infty$ and the wake efficiency $\eta_{\mathrm{w}} = P_{\mathrm{tot}}/(N_{\mathrm{t}}P_1)$, which respectively compare first-row power (P_1) to isolated power (P_∞) and average farm power ($P_{\mathrm{tot}}/N_{\mathrm{t}}$) to first-row power ($P_1$). Additionally, Lanzilao and Meyers (2024) found a strong negative correlation between Δp_{u} and η_{nl}, and a strong positive correlation between Δp_{f} and η_{w}. In SBL conditions, Allaerts and Meyers (2018) found that upstream flow deceleration due to blockage reduced overall farm efficiency, $\eta_\mathrm{f} = \eta_\mathrm{nl}\eta_\mathrm{w}$. In contrast, under CNBL, the favourable pressure gradient can offset upstream losses, potentially improving efficiency compared to fully neutral, non-stratified cases (Lanzilao and Meyers, 2024).

The third type of stratified boundary layer is the convective boundary layer (CBL), which often develops offshore when cold air from a land surface is advected over a relatively warmer sea surface, a phenomenon known as a cold air outbreak. The CBL is characterised by large, coherent structures whose form depends on the degree of atmospheric instability. Salesky et al. (2017) identified three types of convective organisation in their LES study and related their occurrence to the stability parameter $-H/L_\mathrm{ob}$. Here H is the CBL height and

$$L_\mathrm{ob} = -\frac{u_*^3\theta_\mathrm{s}}{\kappa g q_\mathrm{w}} \qquad (1)$$

is the Obukhov length, where u_* is the friction velocity, θ_s is the sea surface temperature, κ is the von Kármán constant and q_w is the surface kinematic heat flux. They found convective rolls for $0 < -H/L_\mathrm{ob} \lesssim 9.8$, intermediate structures for $9.8 \lesssim -H/L_\mathrm{ob} \lesssim 25$, and convective cells for $25 \lesssim -H/L_\mathrm{ob}$.

Relatively little attention has been given to wind farm performance within the convective boundary layer (CBL). This may be due in part to early studies of single turbines in CBLs, which demonstrated significantly improved wake recovery resulting from the enhanced mixing of convective structures (Wen et al., 2013), so that later research has focused primarily on neutral and stable conditions, which are more detrimental to farm efficiency. The improved wake recovery in CBLs could potentially reduce the wind farm presence, and thus the blockage effect. However the findings by Allaerts and Meyers (2018), Lanzilao and Meyers (2024) and Delvaux and Meyers (2025) indicate a pronounced influence of gravity waves and blockage effects, suggesting that these phenomena are likely to persist under convective boundary layer (CBL) conditions. Recent numerical studies investigating wind farms in convective boundary layers (CBLs) (Maas and Raasch, 2022; Souaiby and Porté-Agel, 2025) have identified the presence of hydrostatic blockage and gravity waves. The present work focuses on this blockage effect, emphasizing the influence of induced pressure gradients on individual turbine performance and total wind farm efficiency.

The study is conducted by performing large-eddy simulations (LES) of wind farms operating under convective boundary layer (CBL) conditions. The CBL is generated through a cold-air outbreak, as illustrated in Fig. 1. To reproduce such an outbreak, a CNBL is first initialized over land and then advected over a warmer ocean surface. The surface temperature difference is defined as $\Delta\theta = \theta_\mathrm{l} - \theta_\mathrm{s}$, while a simultaneous jump in surface roughness is introduced as $\Delta z_0 = z_{0,\mathrm{l}} - z_{0,\mathrm{s}}$, where the subscripts l and s denote land and sea, respectively. The range of $\Delta\theta$ considered across the simulations is sufficiently broad to reproduce the three convective regimes identified by Salesky et al. (2017). The article is organised as follows. Section 2 describes the LES framework and simulation setup. Section 3 then presents the LES results for the CBL in the absence of a wind farm, followed by an analysis of the wind farm's interaction with the CBL in Sect.4. Finally, the conclusions are provided in Section 5.

https://doi.org/10.5194/wes-2026-49
Preprint. Discussion started: 31 March 2026

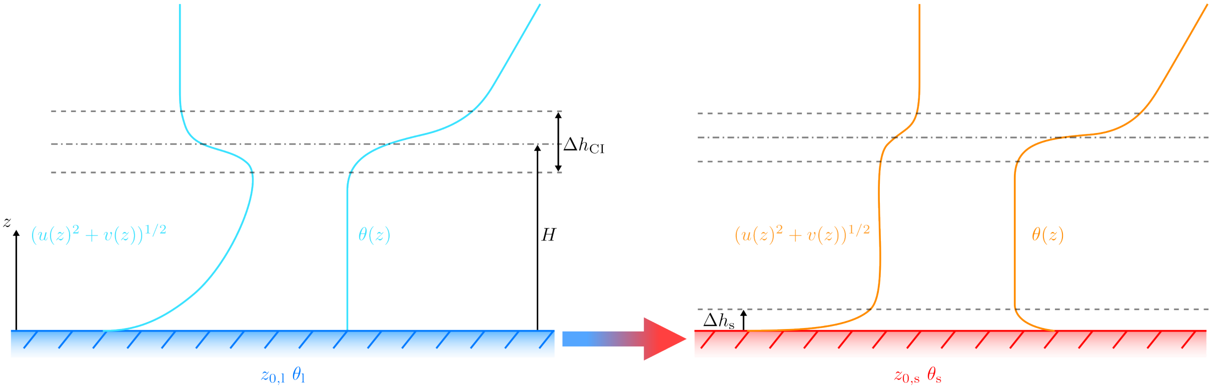

Figure 1. Schematic containing the velocity and temperature profiles during cold air outbreak. The left figure represents the flow over land simulated in our computational domain~~.~~ over a time interval $0 \rightarrow \Delta t_{\mathrm{l}}$. The left figure represents the flow over sea simulated afterwards within the same domain over a time interval $\Delta t_{\mathrm{l}} \rightarrow \Delta t_{\mathrm{l}} + \Delta t_{\mathrm{s}}$.

2 Methodology

2.1 Governing equations

We utilise the incompressible filtered Navier–Stokes equations using the Boussinesq approximation, along with a transport equation for potential temperature, to examine the flow within and surrounding a large-scale wind farm. The governing equations are,

$$\frac{\partial \tilde{u}_i}{\partial x_i} = 0, \tag{2}$$

$$\frac{\partial \tilde{u}_i}{\partial t} + \tilde{u}_j \frac{\partial \tilde{u}_i}{\partial x_j} = f_c \epsilon_{ij3} \tilde{u}_j + \delta_{i3} g \frac{\tilde{\theta} - \theta_l}{\theta_l} - \frac{1}{\rho_0} \frac{\partial p_\infty}{\partial x_i} - \frac{1}{\rho_0} \frac{\partial \tilde{p}^*}{\partial x_i} - \frac{\partial \tau_{ij}^{\mathrm{sgs}}}{\partial x_j} + f_i^{tot}, \tag{3}$$

$$\frac{\partial \tilde{\theta}}{\partial t} + \tilde{u}_j \frac{\partial \tilde{\theta}}{\partial x_j} = -\frac{\partial q_j^{\mathrm{sgs}}}{\partial x_j}, \tag{4}$$

where, the horizontal directions are represented by $i = 1, 2$, and the vertical direction by $i = 3$. The Kronecker delta is denoted by δ_{ij}, and the Levi–Civita symbol by ϵ_{ijk}. The filtered velocity components and potential temperature are indicated by $\tilde{u}_i$ and $\tilde{\theta}$, respectively.

The first term on the right-hand side of eq. 3, represents the Coriolis force resulting from the Earth's rotation, where $f_c = 0.0114\ \mathrm{s}^{-1}$ the Coriolis parameter, corresponding to a latitude of $\phi = 51.6°$. The second term accounts for the thermal buoyancy, with $g = 9.81\ \mathrm{ms}^{-2}$ the gravitational constant and $\theta_{\mathrm{l}} = 288.15$ K the constant reference land surface temperature. The third term corresponds to the steady background pressure gradient that drives the flow across the domain in the horizontal direction, and is linked to the geostrophic wind $G = 10\ \mathrm{ms}^{-1}$ via the geostrophic balance. The fourth term represents the pressure perturbations superimposed on p_∞. The effects of unresolved scales are modelled by the subgrid-scale stress tensor τ_{ij}^{sgs} and the subgrid-scale heat flux q_j^{sgs}. The last term $f_i^{\mathrm{tot}} = f_i + f_i^{\mathrm{ra}} + f_i^{\mathrm{fr}}$ includes all external forces acting on the flow. Specifically,

f_i^{ra} denotes the body force applied within the Rayleigh damping layer (see Sec. 2.2) and f_i^{fr} is the body force applied within the fringe region, which is used to impose inflow boundary conditions in our pseudo-spectral discretization (see Sect. 2.2). The drag force from wind turbines is accounted for by f_i.

The governing equations (2–4) are solved using the SP-Wind solver, an in-house software developed at KU Leuven (Calaf et al., 2010; Goit and Meyers, 2015; Munters et al., 2016; Allaerts and Meyers, 2018; Lanzilao and Meyers, 2024; Delvaux and Meyers, 2025). The equations are integrated over time using a standard fourth-order Runge–Kutta scheme, with the time step determined by a Courant–Friedrichs–Lewy (CFL) number of 0.4. Discretization in horizontal directions is performed using a Fourier pseudo-spectral method, employing the 3/2 dealising rule. In the vertical direction, an energy-preserving fourth-order finite difference scheme is applied Verstappen and Veldman (2003). Continuity is enforced by a direct solve of the Poisson equation at each stage of the Runge–Kutta method. The subgrid-scale motions are modelled with the turbulent kinetic energy (TKE) model Deardorff (1980). This consistent with the SBL study of Allaerts and Meyers (2018) using SP-Wind. We also refer to Calaf et al. (2010); Lignarolo et al. (2016); Martínez-Tossas et al. (2018); Sood et al. (2022) for code benchmarking, and validation.

2.2 Boundary conditions

At the top of the computational domain, a rigid-lid boundary condition is applied to enforce zero vertical velocity, zero shear stress, and a fixed potential temperature. Because this boundary can strongly reflect gravity waves, we include a Rayleigh damping layer (RDL) in the upper free atmosphere, following the approach of Allaerts and Meyers (2017), Lanzilao and Meyers (2023, 2024). The RDL applies a body force proportional to the difference between the local flow and the geostrophic wind, thereby mitigating wave reflection. Periodic boundary conditions are applied along the streamwise and spanwise lateral boundaries. To break the periodicity in the streamwise direction and prescribe inflow conditions, we use the wave-free fringe region technique of Lanzilao and Meyers (2023). A body force is introduced to generate the desired inlet flow, while damping of vertical momentum above the atmospheric boundary layer (ABL) suppresses spurious gravity waves associated with this forcing. This method is used in combination with a concurrent precursor simulation, which continuously supplies a fully developed turbulent inflow field. Finally, periodic boundary conditions are applied along the streamwise and spanwise lateral boundaries, effectively modeling an infinitely wide domain provided that farm-induced disturbances remain confined within the domain interior.

2.3 Atmospheric state

A similar approach as Lanzilao and Meyers (2024) was followed to identify a representative set of atmospheric CBL conditions. We examined 3 years (2021–2023) of ERA5 reanalysis data during winter months, at coordinates 51.6°N, 3.0°E, corresponding to the grid point nearest to the Belgian–Dutch offshore wind farm cluster. The vertical profiles of potential temperature, extending from the surface up to 2.5 km, were fitted using the surface extended Rampanelli Zardi model (SERZ) described by Jamaer et al. (2023), employing a least-squares approach across all levels within this height range. The outputs of this model consist of an estimate of the capping-inversion height H, strength $\Delta\theta_{\mathrm{CI}}$, thickness Δh_{CI} and the lapse rate Γ in the free atmosphere. Additionally we also extracted the sea surface temperature θ_s directly from the ERA5 data and subtract it from the SERZ model output, the mixed-layer temperature θ_m, to obtain the surface temperature jump $\Delta\theta = \theta_\mathrm{l} - \theta_\mathrm{s}$ where $\theta_\mathrm{l} = \theta_\mathrm{m}$. Note that we approximate θ_l to θ_m, but that θ_m in ERA5 may have slightly changed with respect to the land temperature, it originated from. However, establishing this relation in more detail is non-trivial, and we expect this change to be relatively small (e.g. the largest possible change in our simulations yields 1.5 K between initial land conditions and θ_m at beginning of averaging). We grouped the data together into probability density functions to evaluate the relevant states (see Fig. 2). We chose $H = 480,\ 980$ m, $\Delta\theta_\mathrm{CI} = 6$ K, $\Delta h_\mathrm{CI} = 300$ m, $\Gamma = 5$ K km^{-1} and $\Delta\theta = 0,\ 3,\ 6,\ 9$ K, where $\Delta\theta = 0$ K is the reference CNBL case. This results in a total of eight simulation cases listed in Table 2. The case names are designated as HX–$\Delta\theta$Y, where X denotes the initial boundary layer height of the CNBL and Y represents the surface temperature difference. The same geostrophic wind $G = 10$ m s^{-1} was chosen as in Lanzilao and Meyers (2024). In order to appraise the realism of our LES simulations, Fig. 3 compares the LES precursor temperature profiles (1 h time average) to the ERA5 data that fall within the red squares of Fig. 2.

2.4 Simulation setup

The wind farm and numerical domain setup closely follow the simulations by Delvaux and Meyers (2025). An overview is provided in Table 1 and Fig. 4. We first simulate a CNBL in a smaller precursor domain $L_\mathrm{x}^\mathrm{p} \times L_\mathrm{y}^\mathrm{p} \times L_\mathrm{z}^\mathrm{p} = 10 \times 10 \times 25$ km^3, representing the flow over the land surface, with surface roughness length $z_{0,\mathrm{l}} = 1 \times 10^{-2}$ m. The velocity field is initialised from a log-profile, with friction velocity $u_* = 0.28$ m s^{-1}, connected to a laminar geostrophic wind $G = 10$ m s^{-1} above the capping inversion. The initial CNBL potential temperature profiles are generated using Rampanelli and Zardi (2004) (REZ), based on the parameters from Sec. 2.3 (excluding $\Delta\theta$). A statistical steady state is obtained after $\Delta t_\mathrm{l} = 16$ h. The resulting field is then used to initialize the CBL simulations over a sea surface with $z_{0,\mathrm{s}} = 1 \times 10^{-4}$ m, after horizontally extending the turbulent fields to match the main and concurrent precursor domain sizes using the tiling method of Sanchez Gomez et al. (2023).

At $t = 16$ h, the surface boundary conditions are instantly modified to simulate the transition of a statistical steady-state CNBL onto the sea surface. This transition involves a shift in surface roughness to $z_{0,\mathrm{s}} = 1 \times 10^{-4}$ m, while the surface temperature is adjusted such that $\theta_\mathrm{s} = \theta_\mathrm{l} + \Delta\theta$. The study investigates three moderate temperature differences ($\Delta\theta = 0, 3,$ and 6 K) and one extreme case ($\Delta\theta = 9$ K), with $\Delta\theta = 0$ K serving as the reference CNBL. The sea surface temperature remains fixed, while the overlying air mass travels across the sea and gradually warms up until a new steady-state CNBL is established. Time constraints prevent the simulations from ever reaching this new CNBL state. Consequently, the CBL exhibits a slow transient evolution, characterized by a gradual increase in the boundary layer height H and a decrease in the surface kinematic heat flux q_w (see Sect. 3). Despite this transience, the simulations reach a period of constant stability, defined by the parameter $-H/L_\mathrm{ob}$, after approximately 1.5 hours of spin-up. During this interval, the velocity profiles shift from the super-geostrophic jet characteristic of the CNBL to the well-mixed profiles typically found in a CBL. Concurrently, quasi-linear vertical heat flux profiles emerge, while vertical momentum profiles show a slight increase in magnitude within the boundary layer. A spin-up period of $\Delta t_\mathrm{s,spin\text{-}up} = 1.5$ h, after Δt_l, is established to account for the transition from CNBL to CBL, during which

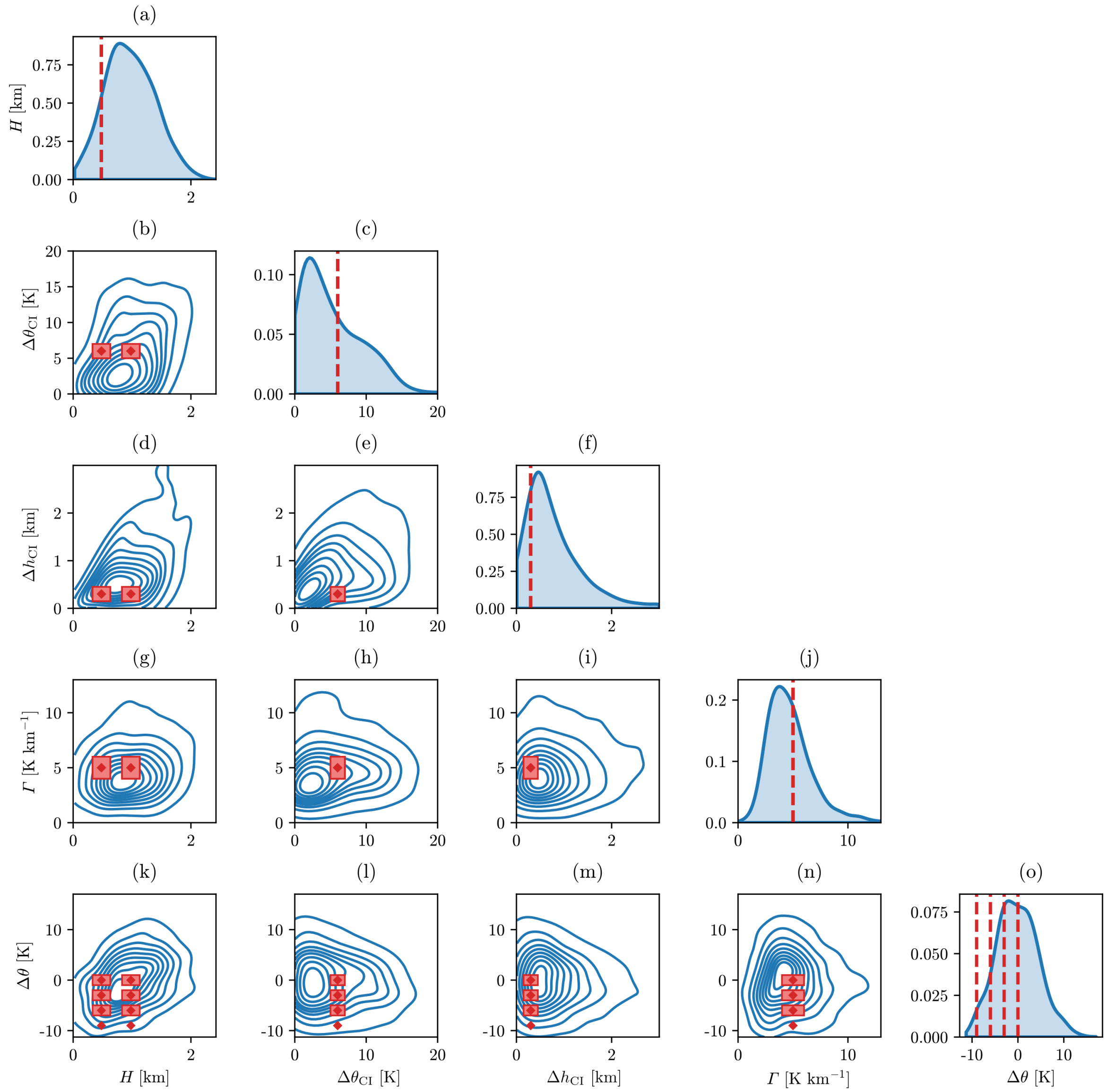

Figure 2. Joint probability density function of the capping-inversion height H, capping-inversion strength $\Delta\theta_{\mathrm{CI}}$, capping-inversion thickness Δh_{CI}, free-atmosphere lapse rate Γ and surface temperature difference $\Delta\theta = \theta_{\mathrm{l}} - \theta_{\mathrm{s}}$. The parameters that characterize the CBL profile are obtained by fitting the ERA5 vertical potential-temperature profile between the surface level and 2.5 km using the surface extended Rampanelli & Zardi model (Jamaer et al., 2023). The red vertical dashed lines and diamonds denote the parameters selected in the current study, i.e. $H = \{480,\ 980\}$ m, $\Delta\theta_{\mathrm{CI}} = \{6\}$ K, $\Delta h_{\mathrm{CI}} = \{300\}$ m, $\Gamma = \{5\}$ K km^{-1} and $\Delta\theta = \{0,\ 3,\ 6,\ 9\}$ K. The red rectangles mark the parameter space for the temperature profiles illustrated in Fig. 3. All combinations are considered, for a total of 8 cases.

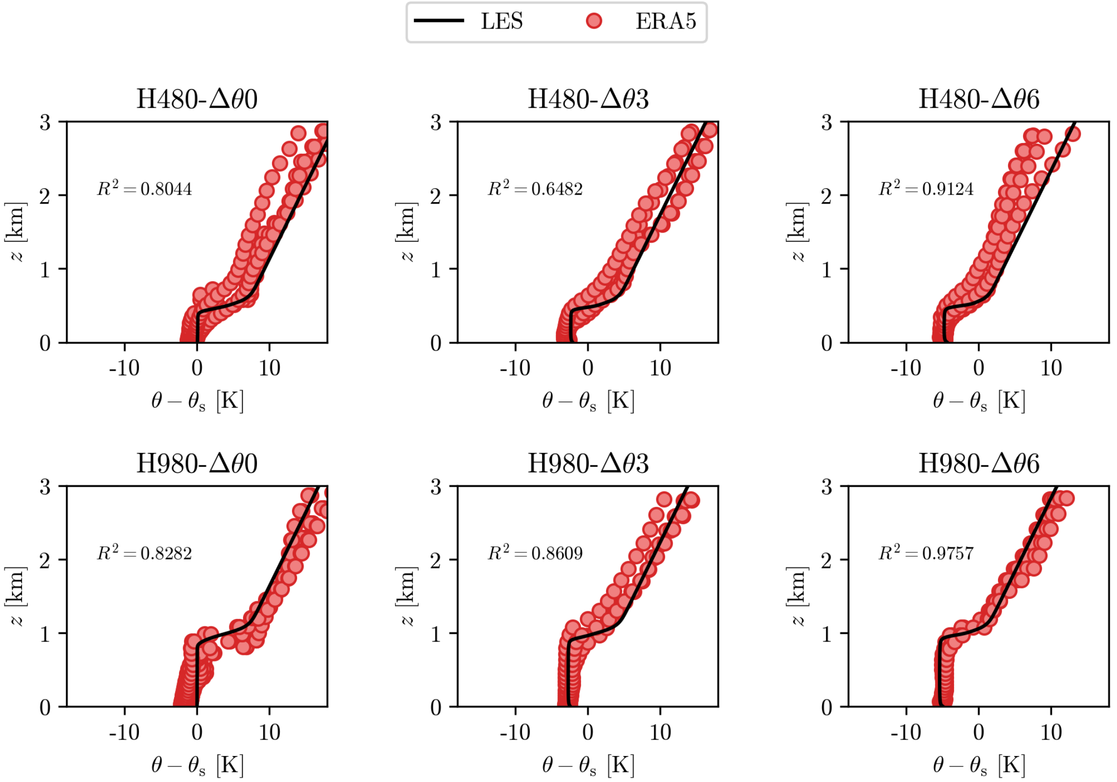

Figure 3. Comparison of vertical potential temperature profiles between LES and ERA5 re-analysis data. The solid black lines represent 1 h time-averaged LES results, while the red dots indicate five ERA5 profiles selected from the red rectangle parameter space defined in Fig. 2. The subplots display results for $H = \{480,\ 980\}$ m and $\Delta\theta = \{0,\ 3,\ 6\}$ K. The R^2 value denotes the coefficient of determination.

vertical profiles undergo drastic adjustments. Following this spin-up phase, the profiles exhibit significantly less variation over the subsequent hour. Therefore, the statistical analysis is conducted within this following time window $\Delta t_{\mathrm{s,main}} = 1$ h. When translating this temporal setup to a spatial framework, the 1.5-hour transition period corresponds to an equivalent fetch distance of 54 km, assuming a direction velocity equal to the geostrophic wind $G = 10$ m s^{-1}.

2.5 Wind farm specifications

The main specifications are listed in Table 1. We consider a 1.5 GW offshore wind farm consisting of $N_\mathrm{t} =$ 100 IEA 15 MW turbines, arranged in a staggered layout with 10 rows (N_t^x) and 10 columns (N_t^y) (see Table 1). The turbines have a rotor diameter $D = 240$ m and a hub height $z_\mathrm{h} = 150$ m. The farm spans 12 km in both directions ($L_\mathrm{f}^\mathrm{x} = L_\mathrm{f}^\mathrm{y} = 12$ km), with a streamwise and spanwise turbine spacing $S_\mathrm{x} = S_\mathrm{y} = 5D$. To mitigate artificially induced domain blockage, we follow Lanzilao and Meyers (2024) guidelines, such that the ratios $L_\mathrm{up}/L_\mathrm{f}^\mathrm{x}$, $L_\mathrm{x}/L_\mathrm{f}^\mathrm{x}$, and $L_\mathrm{y}/L_\mathrm{f}^\mathrm{y}$ are 1.5, 4.17, and 3.34, respectively.

Table 1. Setup of the computational domain and wind farm

Main domain size	$L_\mathrm{x} \times L_\mathrm{y} \times L_\mathrm{z} = 50\ \mathrm{km} \times 40\ \mathrm{km} \times 25\ \mathrm{km}$
Concurrent precursor domain size	$L_\mathrm{x} \times L_\mathrm{y} \times L_\mathrm{z} = 10\ \mathrm{km} \times 40\ \mathrm{km} \times 25\ \mathrm{km}$
Main domain grid	$N_\mathrm{x} \times N_\mathrm{y} \times N_\mathrm{z} = 1240 \times 992 \times 245$
Concurrent precursor domain grid	$N_\mathrm{x} \times N_\mathrm{y} \times N_\mathrm{z} = 248 \times 992 \times 245$
Vertical grid	$\begin{cases} N_{\mathrm{z},1} = 150, & \Delta z = 10\ \mathrm{m}, \quad 0 < z < 1.5\ \mathrm{km} \\ N_{\mathrm{z},2} = 90, & \Delta z = 10 - 600\ \mathrm{m}, \quad 1.5 < z < 15\ \mathrm{km} \\ N_{\mathrm{z},3} = 5, & \Delta z = 600 - 3500\ \mathrm{m}, \quad 15 < z < 25\ \mathrm{km} \end{cases}$
Horizontal grid resolution	$\Delta x = \Delta y = 40.3$ m
Turbine arrangement	10 rows × 10 columns
Turbine dimensions	$D = 150$ m and $z_\mathrm{h} = 150$ m
Turbine spacing	$S_\mathrm{x} = S_\mathrm{y} = 5D$ and $10D$

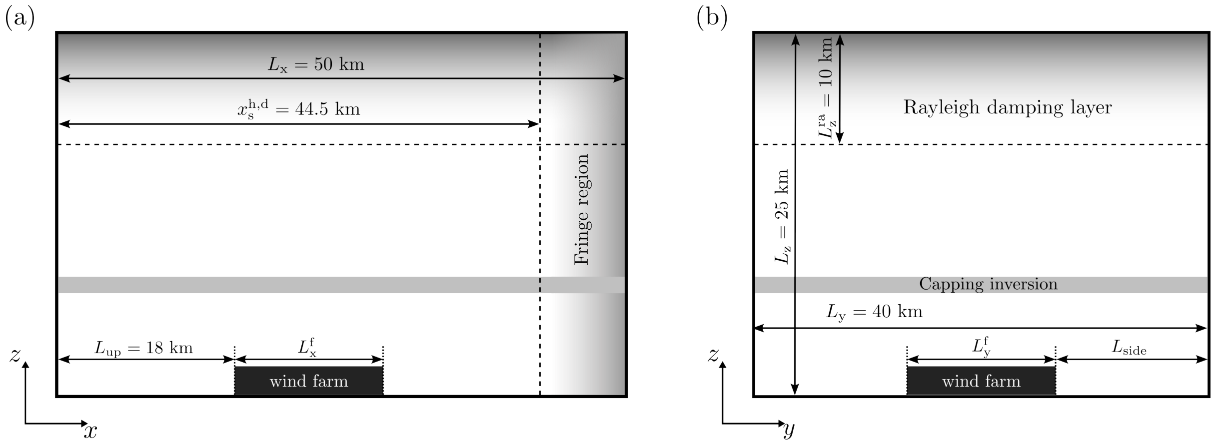

Figure 4. Side (a) and front (b) view of the computational domain. The figure is reproduced from Delvaux and Meyers (2025).

Since the turbines operate below their rated power under the given conditions, we adopt a constant disc-based thrust coefficient $C_\mathrm{T}' = 1.44$, which corresponds to $C_\mathrm{T} = 0.778$ in the constant thrust region as obtained from the IEA 15 MW reference report (Gaertner et al., 2020a, b). Moreover, a simple yaw controller is implemented to keep all turbine rotor discs perpendicular to the incident wind flow measured one rotor diameter upstream. Similar to Delvaux and Meyers (2025), the turbine forces (per unit of density) are modelled using a non-rotating actuator disc model (Meyers and Meneveau, 2010) with a Shapiro correction factor (Shapiro et al., 2019) to avoid over prediction of turbine power on typical LES grid resolutions.

The wind farm is simulated across each atmospheric state defined in Sec. 2.3. To calculate farm efficiencies, four additional stand-alone turbine simulations are performed for each wind farm case within its corresponding atmospheric environment.

Table 2. Overview of the concurrent precursor simulations that drive the wind farm simulations. The parameters are averaged over 1 h after 1.5 h spin-up phase and include the capping-inversion height H, the land-sea temperature difference $\Delta\theta$, the horizontal velocity magnitude at hub height M_{hub}, the turbulence intensity measured at hub height $\mathrm{TI}_{\mathrm{hub}}$, the friction velocity u_*, the convective velocity scale $w_* = (gq_{\mathrm{w}}H/\theta_{\mathrm{s}})^{1/3}$ and the Obukhov length L_{ob}.

Cases	H [m]	$\Delta\theta$ [K]	M_{hub} [ms^{-1}]	$\mathrm{TI}_{\mathrm{hub}}$[%]	u_* [ms^{-1}]	w_* [ms^{-1}]	$-H/L_{\mathrm{ob}}$ [-]
H480-$\Delta\theta$0	488	0	10.10	3.02	0.26	0	0
H480-$\Delta\theta$3	499	2	9.88	4.46	0.32	0.76	5.41
H480-$\Delta\theta$6	512	6	9.79	5.57	0.33	0.99	11.22
H480-$\Delta\theta$9	526	9	9.75	6.41	0.33	1.16	17.38
H980-$\Delta\theta$0	981	0	9.62	3.63	0.27	0	0
H980-$\Delta\theta$3	988	2	9.97	5.76	0.33	1.00	11.61
H980-$\Delta\theta$6	997	6	9.95	7.19	0.34	1.30	23.2
H980-$\Delta\theta$9	1008	9	9.91	8.27	0.34	1.51	35.11

160 Across these four simulations, the position of the stand-alone turbine is shifted by a distance $L_{\mathrm{x}}^{\mathrm{p}}/4$ to mitigate dependence on the spatial heterogeneity of the convective flow.

3 Precursor simulations

Figure 5 shows the temporal evolution of the horizontally averaged turbulence intensity at hub height, the boundary layer height (H) and the stability parameter $(-H/L_{\mathrm{ob}})$, for the concurrent precursor simulation including spin-up and main phase. The 165 effect of the surface temperature difference is clearly visible. A bigger surface temperature jump results in stronger convective structures, which leads to a higher $\mathrm{TI}_{\mathrm{hub}}$ and $-H/L_{\mathrm{ob}}$. Increasing the boundary layer height has the same effect. Therefore, H980-$\Delta\theta$9 is the atmospheric state with the strongest turbulence intensity and stability parameter. We note that during the spin-up phase both TI and $-H/L_{\mathrm{ob}}$ change drastically, as the transition from CNBL to CBL occurs. During the main simulation phase, the parameters remain constant, similar to the CBL simulations of Lu and Porté-Agel (2015).

170 The horizontally and time-averaged vertical profiles, calculated over a 1 h interval for the concurrent precursor simulations, are presented in Fig. 6. Specifically, Fig. 6a displays the horizontal velocity magnitude normalized by the geostrophic wind. We observe that in the convective cases ($\Delta\theta > 0$), the horizontal velocity exhibits a more uniform distribution within the ABL, compared to the CNBL case with the presence of a super-geostrophic jet near the top of the ABL. However for H980, the velocity profile differs from the typical CBL profiles, in which the velocity in the boundary layer is smaller than the geostrophic 175 wind as is found for H480. This is due to the surface roughness transition from land $z_{0,\mathrm{l}}$ to sea $z_{0,\mathrm{s}}$, resulting in a flow acceleration in the ABL, which becomes more prominent with increasing ABL height. Figure 6b illustrates the flow angle scaled with the largest absolute geostrophic wind angle $|\alpha|_{\max} = 15.02°$, corresponding to case H480-$\Delta\theta$0. Consistent with the findings of

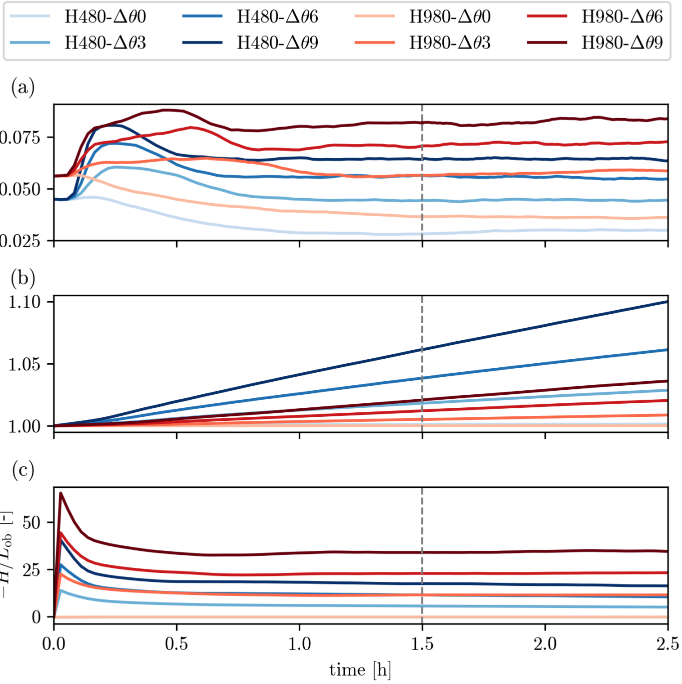

Figure 5. Temporal evolution of (a) the turbulence intensity at hub height, (b) the boundary layer height, normalized by its value at the onset of surface transition and (c) the stability parameter. Results cover the CNBL to CBL transition phase ($t = 0 - 1.5$ h) and the statistical analysis window ($t = 1.5 - 2.5$ h), separated by vertical grey dashed line. The CNBL spin-up phase is not included.

Lanzilao and Meyers (2024), higher ABLs exhibit a smaller $|\alpha|$. Additionally, the convective cases possess significantly less veer, in agreement with the results of Salesky et al. (2017). Figure 6c shows the potential-temperature profiles. The temperature within the shallow ABL approaches θ_s more rapidly than in deeper layers. This occurs because mixing in shallow CBLs is restricted to a shorter vertical distance, as convective structures are constrained by the low capping inversion. Consequently, surface heat is distributed into a smaller volume of air, resulting in a faster temperature increase. Additionally, for cases with the same initial boundary layer height, a larger $\Delta\theta$ leads to more rapid boundary layer growth due to the increased surface heating. Next, Fig. 6 (d) displays the vertical heat flux, scaled with the largest wall heat flux $q_{\mathrm{w,max}} = 3.47 \times 10^{-4}$ K m s^{-1}, corresponding to case H980-Δθ9. For the convective cases, the heat flux is only non-zero below the top of the capping-inversion, with a nearly linear profile within the ABL. We note that the large ABLs have a larger q_{w} than their corresponding lower ABLs. This is due to the faster temperature transition for the lower ABLs, resulting in a smaller temperature difference between the air and the surface. Finally, Fig. 6 (d) displays the shear stress magnitude scaled with the largest friction velocity $u_{*,\mathrm{max}} = 0.33$ m s^{-1}, corresponding to case H980-Δθ6. A quasi-linear profile is found below the capping-inversion for all cases, similar to Lanzilao and Meyers (2024). We note that the shear stress magnitude is non-zero in the free atmosphere for the CBL cases, unlike the CNBL cases. We suspect this vertical flux of horizontal momentum to be the wave stress defined in Nappo (2012), associated

https://doi.org/10.5194/wes-2026-49
Preprint. Discussion started: 31 March 2026

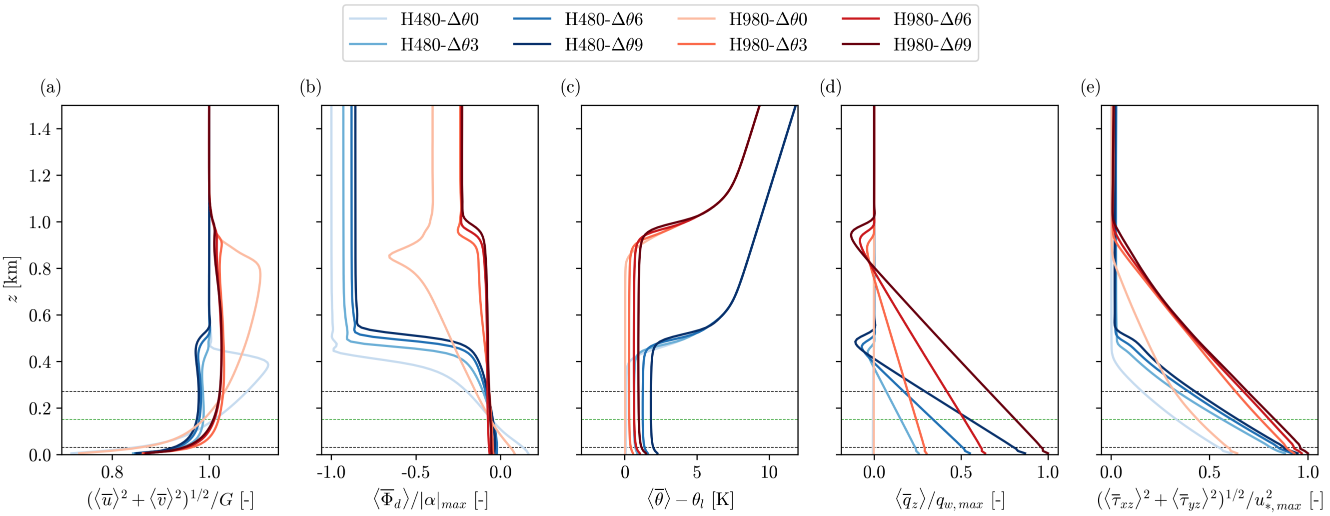

Figure 6. Vertical profiles of (a) velocity magnitude, (b) wind direction, (c) potential temperature, (d) kinematic heat flux and shear stress magnitude averaged along the full horizontal directions and over 1 h in the concurrent precursor domain. The profiles are further normalized with $G = 10$ m s^{-1}, $|\alpha|_{\max} = 15.02°$, $\theta_{\mathrm{l}} = 288.15$ K, $q_{\mathrm{w,max}} = 3.47 \times 10^{-4}$ K m s^{-1} , $u_{*,\max} = 0.34$ m s^{-1}.

with vertically propagating gravity waves. These gravity waves are induced by the presence of the convective structures inside the CBL (Wulfmeyer et al., 2016). A similar profile above the capping inversion was found in the convective boundary layers of Maas and Raasch (2022). We do remark that the wave stress, with the associated gravity waves, are significantly weaker than the stationary waves that are excited when considering the presence of the wind farm.

4 Impact of atmospheric conditions on wind farm performance

In the following analysis, results are presented as 1 h time-averaged quantities unless stated otherwise. For the sake of conciseness, the overbar notation $(\overline{\cdot})$ is omitted, and time-dependent variables are explicitly identified where they appear.

4.1 Comparison of flow profiles

Figures 7 and 8 show the instantaneous streamwise and vertical velocity fields for all the tested atmospheric conditions. In the vertical velocity fields, increasing $\Delta\theta$ leads to stronger up- and downdrafts far from the wind farm, reflecting the formation of convective structures. These vertical velocities are significantly stronger than the vertical velocities inside the turbine and farm wake. In the streamwise velocity fields, we observe for $\Delta\theta = 0$ the typical flow acceleration at the wind farm sides due to blockage. As $\Delta\theta$ increases, this flow speed-up becomes less pronounced due to enhanced vertical mixing. To better visualize the convective structures, Fig. 9 shows a zoomed-in region of the concurrent precursor. Following the classification framework of Salesky et al. (2017), we identify three distinct convective regimes: rolls in cases H480-Δθ3 and H980-Δθ3; intermediate

https://doi.org/10.5194/wes-2026-49
Preprint. Discussion started: 31 March 2026

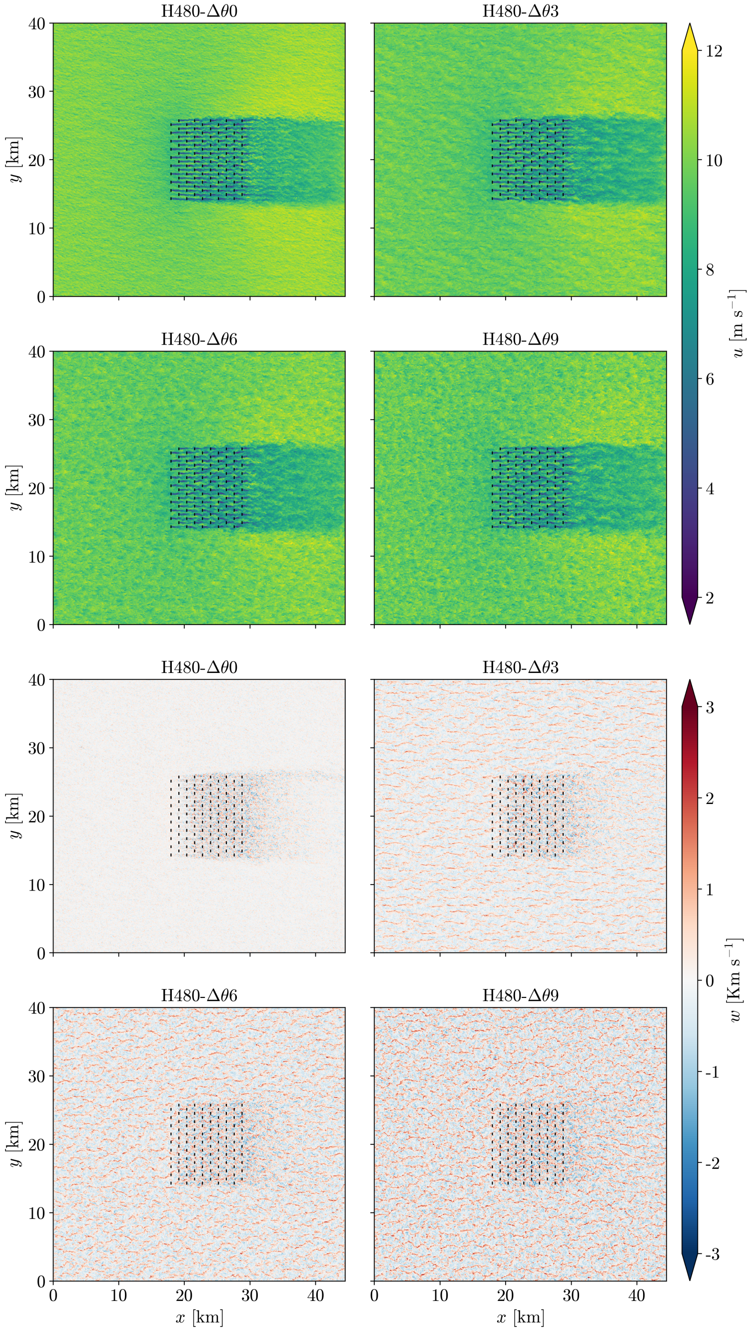

Figure 7. Instantaneous streamwise (u) and vertical (w) velocity fields at hub height for cases with $H = 480$ m. Turbine locations are indicated by black markers.

https://doi.org/10.5194/wes-2026-49
Preprint. Discussion started: 31 March 2026

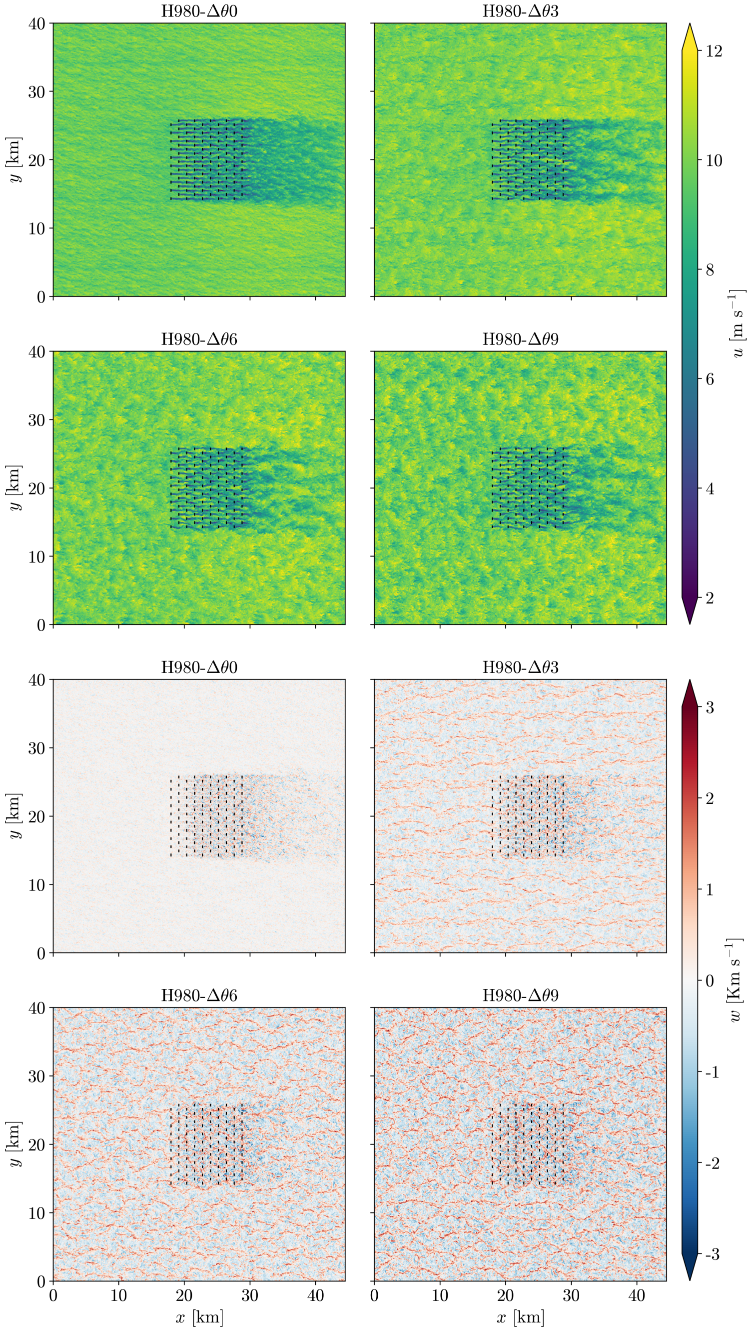

Figure 8. Instantaneous streamwise (u) and vertical (w) velocity fields at hub height for cases with $H = 980$ m. Turbine locations are indicated by black markers.

https://doi.org/10.5194/wes-2026-49
Preprint. Discussion started: 31 March 2026

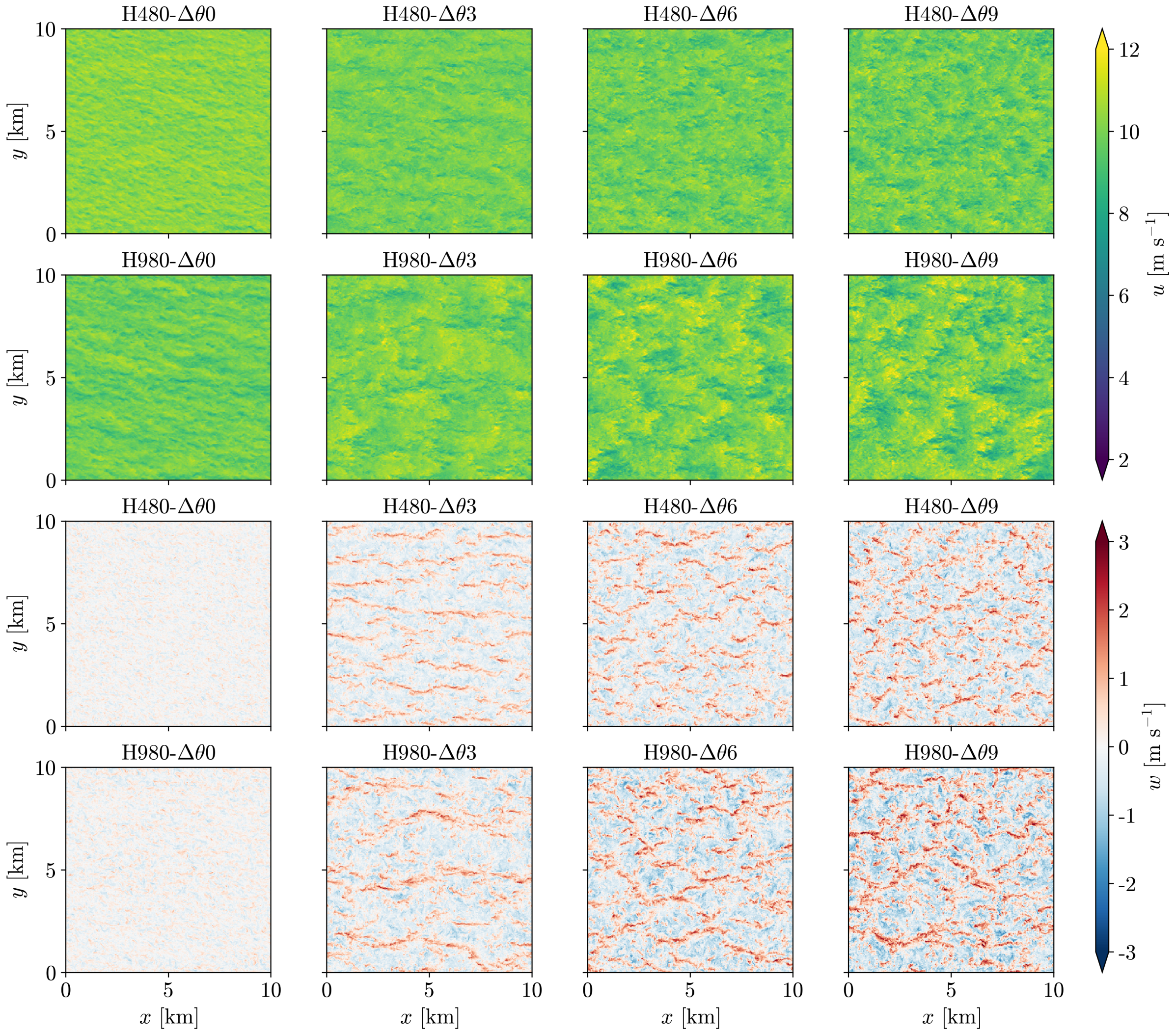

Figure 9. Instantaneous streamwise (u) and vertical (w) velocity fields of the precursor at hub height for all cases.

structures in H480-$\Delta\theta$6 and H480-$\Delta\theta$9; and cells in H980-$\Delta\theta$6 and H980-$\Delta\theta$9. Our calculated stability parameters ($-H/L_{\text{ob}}$) somewhat align with their reported intervals, although minor discrepancies likely arise from our use of a fixed sea surface temperature (θ_{s}) rather than a prescribed heat flux. In further agreement with their observations, these structures remain visible in the streamwise velocity as alternating high- and low-speed patches. 210

Convective structures are typically characterized by their wavelength (λ), representing either the cell diameter or twice the roll diameter; along with the boundary layer height (H) and the resulting aspect ratio (λ/H). Using a spatial Fourier transform of the vertical velocity field, we identify characteristic scales of $\lambda \approx 1.1$–1.2 km ($\lambda/H \approx 2.5$) for the shallow CBL cases,

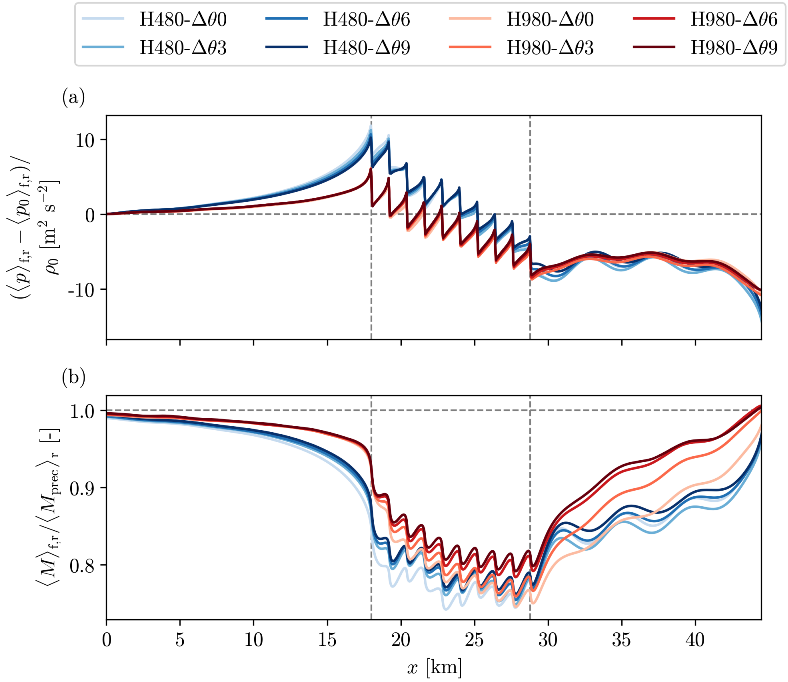

Figure 10. Time-averaged (a) pressure perturbation (b) horizontal velocity magnitude averaged over the farm width and turbine rotor height as a function of the streamwise direction. The vertical dashed grey lines denote the location of the first- and last-row turbines.

and $\lambda \approx 3.2$–3.3 km ($\lambda/H \approx 3.3$) for the deep CBL cases. These values align with the limited aspect ratios observed for convective structures in numerical simulations of dry boundary layers (Deardorff, 1972). While these sizes are consistent with observations of cloudless convective boundary layers, satellite imagery also reveals significantly larger structures with aspect ratios reaching up to 40 (Atkinson and Wu Zhang, 1996). Capturing the horizontal expansion of such large-scale structures requires the inclusion of a moisture transport equation to account for cloud formation, cloud-top radiative cooling, and latent heat release (Müller and Chlond, 1996).

We now investigate and compare the flow profiles across all cases. The results are presented in Fig. 10, which illustrates the flow profiles averaged over time and farm width, as a function of the streamwise coordinate. Figure 10a shows the pressure perturbation averaged over the farm width and turbine rotor height minus the pressure at the domain entrance. Across all atmospheric states, the presence of the wind farm induces an unfavourable pressure gradient (Δp_{u}) upstream, followed by a favourable pressure gradient (Δp_{f}) within the farm. We observe that shallow boundary layer cases possess stronger pressure gradients, as well as higher amplitude perturbations downstream of the farm induced by gravity waves, similar to Lanzilao and Meyers (2024). When increasing $\Delta\theta$, we observe a slight decrease in both pressure gradient magnitudes $|\Delta p_{\mathrm{u}}|$ and $|\Delta p_{\mathrm{f}}|$. However, this sensitivity is only noticeable for shallow boundary layers. This behavior likely stems from the relatively larger increase in H observed in shallow cases as $\Delta\theta$ increases (see Fig. 5b). Figure 10b illustrates the horizontal velocity magnitude averaged over the farm width and turbine rotor height, scaled with the horizontal velocity at hub height from the concurrent precursor. The unfavourable pressure gradient is clearly impactful, as pronounced flow slowdown persists several turbine spacings upstream of the farm in all cases. Following the results from Fig. 10a, slightly less flow slowdown is observed for higher $\Delta\theta$ in shallow boundary layers. Within the farm, velocity recovers considerably faster for more convective conditions, due to the enhanced vertical mixing of the convective structures, and related increase of the turbulence intensity (see Table. 2).

4.2 Wind farm power production

It is now of interest to examine how power is distributed across the wind farm. Figure 11a presents the row-averaged power normalized by the stand-alone turbine power (P_∞), under identical atmospheric conditions. All stability cases have a similar shape for the power distribution. The staggered layout ensures that second-row turbines are not directly exposed to upstream wakes. Consequently, the first two rows are primarily influenced by blockage effects rather than wake interference, resulting in a considerably smaller power deficit relative to the stand-alone turbine, in contrast to the downstream rows. For the deep boundary layer cases (H980), increasing $\Delta\theta$ significantly enhances the normalized power of waked turbines but leaves the first two rows unaffected. This behaviour is consistent with Fig. 10b, which shows accelerated wake recovery within the farm at higher $\Delta\theta$, while the upstream flow slowdown remains identical across all H980 cases. Similar trends are observed for the shallow boundary layer (H480); however, in this regime, the transition from neutral to convective conditions does increase the normalized power of the first two rows. This is further elucidated by Fig. 10b, where the neutral case exhibits a more pronounced flow slowdown upstream of the farm.

Figure 11b shows the row averaged power normalised by the average front row power. Under convective conditions, the power output of waked rows gets closer to the first two rows. This behaviour results from the enhanced wake recovery driven by stronger turbulent mixing, as illustrated in Fig. 10b. The effect is particularly pronounced in the deep boundary layer, where a larger volume of mixing flow is available. However, consistent with the observed wake recovery patterns, the magnitude of this power increase diminishes as $\Delta\theta$ continues to rise. For the neutral cases, we observe a more uniform power distribution across the rows in the shallow boundary layer compared to the deep boundary layer. This is attributed to the presence of a significantly stronger favourable pressure gradient across the farm in the shallow case. However, as $\Delta\theta$ increases and turbulent mixing improves, wind farms in both boundary layer heights converge toward similar power distributions. Overall, comparable power distributions are found in the recent numerical results of Souaiby and Porté-Agel (2025), for wind farms operating in convective conditions.

Figure 11c illustrates the row-averaged local axial induction, defined as $a = 1 - U_\mathrm{d}/U_\mathrm{in}$, where U_d is the rotor-disk-averaged velocity and U_in represents the local turbine inflow velocity. For brevity, the detailed procedure for calculating these local values is provided in Appendix A. Increasing $\Delta\theta$ results in decreasing and increasing local axial induction for the first row and waked rows, respectively. We note that the local axial induction of the waked turbine rows is remarkably smaller than the value of the first two rows. This is predominantly due to the favourable pressure gradient across the farm. This relationship is illustrated in Fig. 12a, which depicts the row-averaged local axial induction against the row-averaged local pressure gradient $\Delta p/L$. A strong positive correlation exists between these two variables, specifically, a more negative (favourable) local pressure gradient is linked to a reduction in local axial induction. This observation aligns with the findings of Ndindayino et al. (2025) and Bleeg (2026). Furthermore, the discrepancy in axial induction between non-waked turbines (rows 1–2, indicated by the green dashed box) and waked turbines (rows 3–10, indicated by the pink dash-dot box) turbines is also influenced by local turbulence intensity. Waked turbines operate within higher TI environments, which contributes to lower axial induction (Revaz and Porté-Agel, 2025). Fig. 12b clarifies this point by plotting row-averaged local axial induction versus row-averaged TI, where the TI of each turbine is averaged over the rotor disk. While the correlation with TI is less pronounced than that of the local pressure gradient, two distinct regimes still emerge: high axial induction associated with low TI (green dashed box) and low axial induction associated with high TI (pink dash-dot box). The weaker correlation suggests that the influence of TI on local axial induction is secondary to the effect of the pressure gradient. Nevertheless, further investigation across a broader parameter space is required to isolate the relative contributions of the pressure gradient and TI to turbine performance.

To further illustrate this point, Fig. 12b shows the row averaged local axial induction versus the disk averaged turbulence intensity averaged over the row. Although the TI is not as well correlated to the axial induction as is the local pressure gradient, we identify two distinct regions of high (green dashed box) and low (pink dash-dot box) axial induction linked to low and high TI respectively. However the worse correlation implies that the effect of the TI on the local axial induction is smaller than the effect of the pressure gradient. Nonetheless, the favourable pressure gradient across the farm induced by blockage, visible in Fig. 10a, significantly impacts turbine performance in the CBL case, mirroring the effects on power distribution observed in the CNBL case.

4.3 Wind farm efficiencies

We now examine the distribution of the power coefficient $C_{\mathrm{P},mn}$ for each turbine within the farm. For a turbine at position mn, where $m \in [1, N_\mathrm{t}^\mathrm{x}]$ and $n \in [1, N_\mathrm{t}^\mathrm{y}]$, the coefficient is defined as:

$$C_{\mathrm{P},mn} = \frac{P_{mn}}{\frac{1}{2}\rho_0 A_\mathrm{d} U_\infty^3}, \tag{5}$$

where P_{mn} represents the generated power, A_d is the rotor disk area, and U_∞ is the undisturbed streamwise velocity. The latter is obtained from the precursor simulation by averaging the velocity within a streamwise cylinder that spans the domain length and envelops the rotor area of turbine mn. Figure 13 shows the C_P distribution for all wind farm cases, where each hexagon represents a single turbine. In accordance with Delvaux and Meyers (2025), a higher boundary layer height H results in larger C_P values across the entire farm. Furthermore, as shown in Fig. 11b, the convective cases exhibit a more uniform power distribution among the turbine rows compared to the CNBL cases. The C_P output of the waked rows (3–10) is much closer to that of the non-waked rows (1–2), due to enhanced wake recovery within the farm, as shown in Fig. 10b.

We extend the analysis to farm-scale efficiencies, shown in Fig. 14, which are defined following Allaerts and Meyers (2018) as

$$\eta_\mathrm{nl} = \frac{P_1}{P_\infty}, \quad \eta_\mathrm{w} = \frac{P_\mathrm{tot}}{N_\mathrm{t} P_1} \quad \text{and} \quad \eta_\mathrm{f} = \eta_\mathrm{nl}\eta_\mathrm{w}. \tag{6}$$

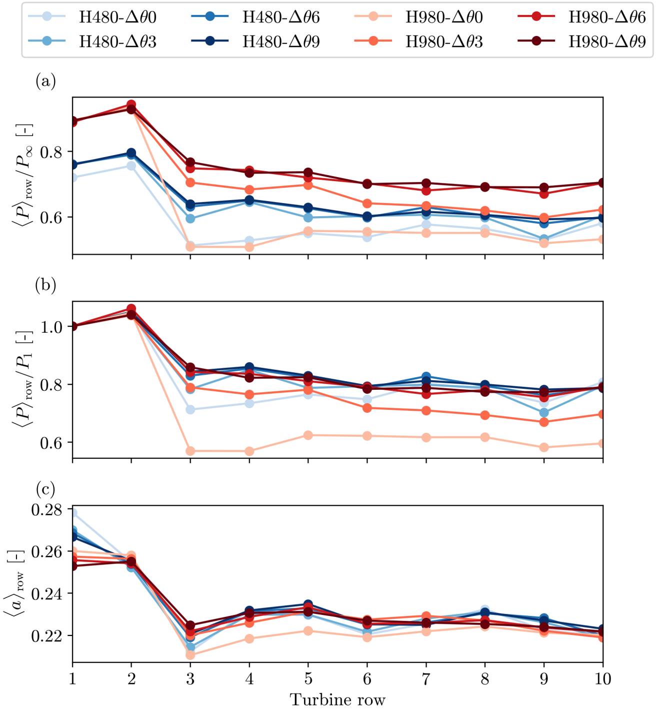

Figure 11. Variation of time- and row-averaged turbine performance across the farm for different stability conditions: (a) turbine power normalized by a stand-alone turbine under equivalent stability, (b) turbine power normalized by the first-row power, and (c) local axial induction factor.

In these expressions, all power terms are 1h times-averages, where P_∞ represents a stand-alone turbine, P_1 is the front row average, and P_{tot} is the total production of the farm consisting of N_{t} turbines. Figure 14a shows that reducing H slightly increases the sensitivity of η_{nl} to $\Delta\theta$. Specifically, for the shallow boundary layer (H480), the transition from neutral to convective conditions yields an increase in η_{nl} of $\sim 5\%$. This can be explained by looking at Fig. 10b, where the neutral case exhibits a more pronounced flow slowdown upstream of the farm. Further increases in $\Delta\theta$ result in a plateau. In contrast, for the deep boundary layer cases (H980), η_{nl} remains insensitive to variations in $\Delta\theta$. This indicates that, similar to wind farms operating inside CNBLs (Lanzilao and Meyers, 2024), blockage remains relevant even in deep boundary layers, where η_{nl} maintains a nearly constant value of approximately 90%. Substantial changes are observed for η_{w}, as illustrated in Fig. 14b. For both boundary layer heights, η_{w} increases with $\Delta\theta$, indicating improved wake recovery under more convective conditions. This trend is more pronounced for H980, where the larger boundary layer contains more mixing flow, enhancing vertical momentum exchange compared to the shallow H480 cases. Note that for the strong convective cases ($\Delta\theta \geqslant 6$ K), η_{w} converges to a nearly identical value for both boundary layer heights. Meaning that the increased convective mixing compensates for the significantly lower favourable pressure gradient in H980. Since variations in η_{w} are significantly larger than those in η_{nl}, the farm efficiency η_{f}

https://doi.org/10.5194/wes-2026-49
Preprint. Discussion started: 31 March 2026

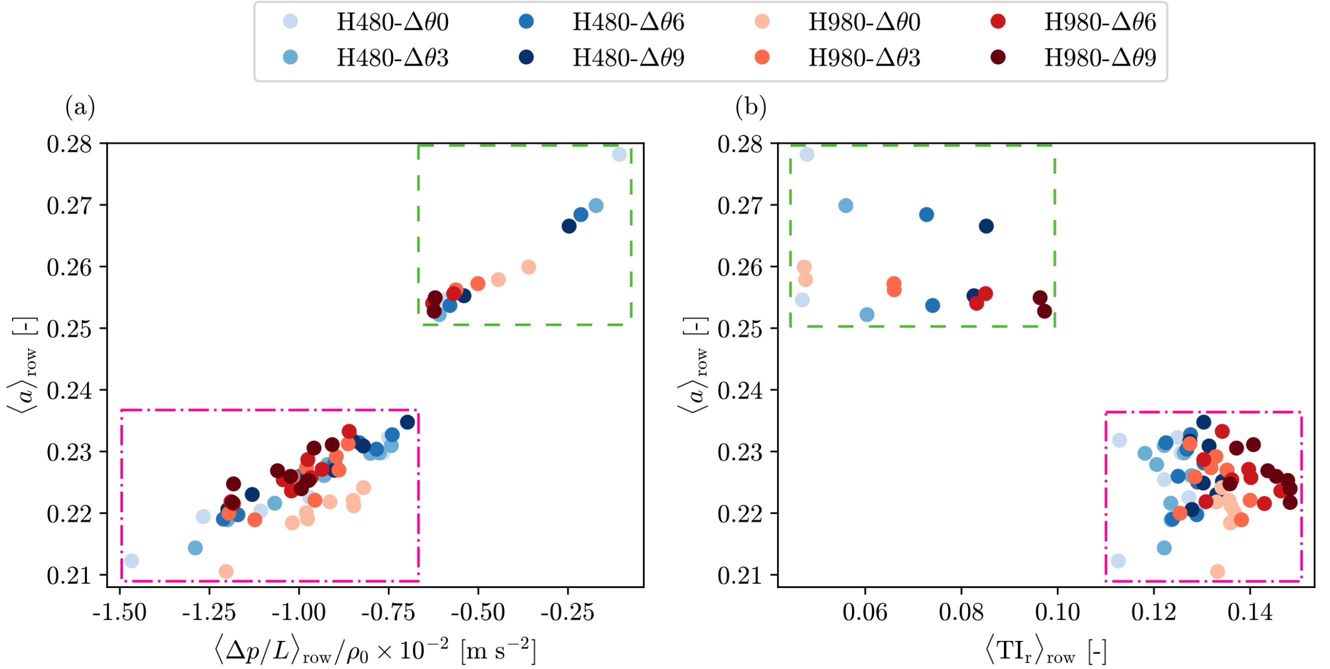

Figure 12. The row-averaged local axial induction (a) as a function of (a) the the row averaged local pressure gradient ($\Delta p/L$) and (b) the row-averaged local turbulence intensity (TI) The green dashed box contains the non-waked rows and the pink dash-dot box contains the waked rows.

primarily follows the trend of η_{w} (Fig. 14c). Furthermore, as $\Delta\theta$ increases, the increase in η_{f} gradually plateaus, indicating a diminishing sensitivity to further increases in $\Delta\theta$. Increasing the boundary layer height for a convective case, results in a larger increase of η_{f} compared to the neutral case. We found the largest increase of $+15\%$ for $\Delta\theta = 9$ K. We conclude that in shallow boundary layers, dominant unfavourable and favourable pressure gradients significantly influence performance, leading to lower non-local efficiencies and higher wake efficiencies, respectively. Conversely, relatively weak mixing in these cases results in less significant changes in wake efficiency as $\Delta\theta$ increases. In deep boundary layer cases, convective mixing is substantially stronger than in shallow boundary layers at the same $\Delta\theta$. Furthermore, because the pressure gradients are noticeably smaller in these deep cases, the influence of convective mixing on wake efficiency becomes more pronounced as $\Delta\theta$ varies.

Based on the local definitions derived in Appendix A and the power production findings in Sec. 4.2, the total farm efficiency η_{f} is further decomposed into four newly defined efficiencies:

$$\eta_{\mathrm{f}} = \Pi_1\Pi_2\Pi_3\Pi_4, \tag{7}$$

with the non-local efficiency $\eta_{\mathrm{nl}} = \Pi_1\Pi_2$ and the wake efficiency $\eta_{\mathrm{w}} = \Pi_3\Pi_4$. To calculate the efficiencies (Π_i), four additional theoretical farm configurations are defined besides the standard farm. First the ideal farm A, where all turbines operate as

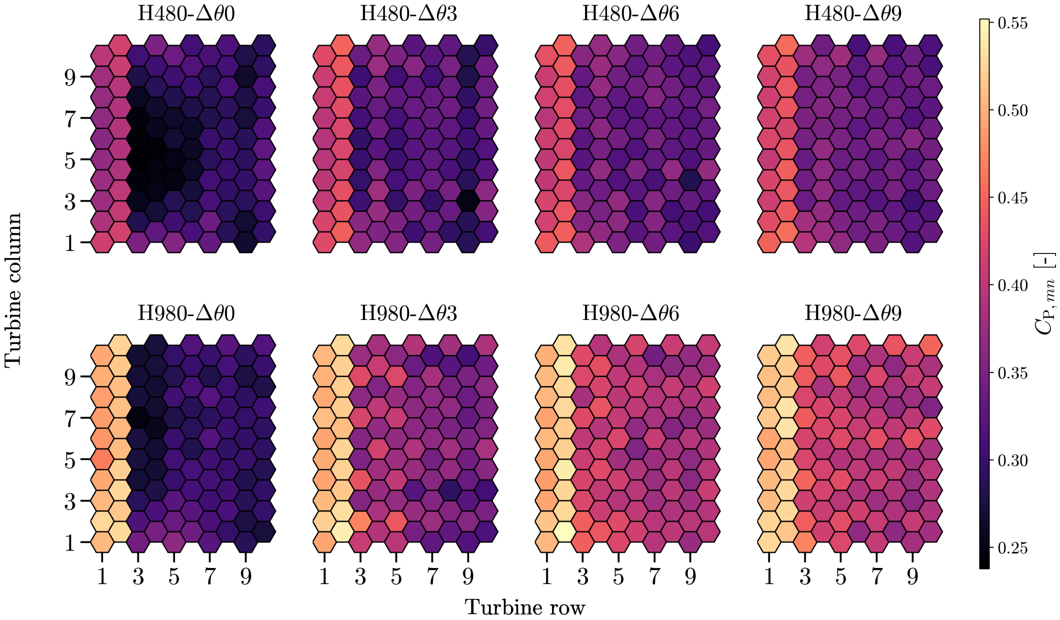

Figure 13. Farm distribution of the turbine power coefficient (C_P) from Eq. (5).

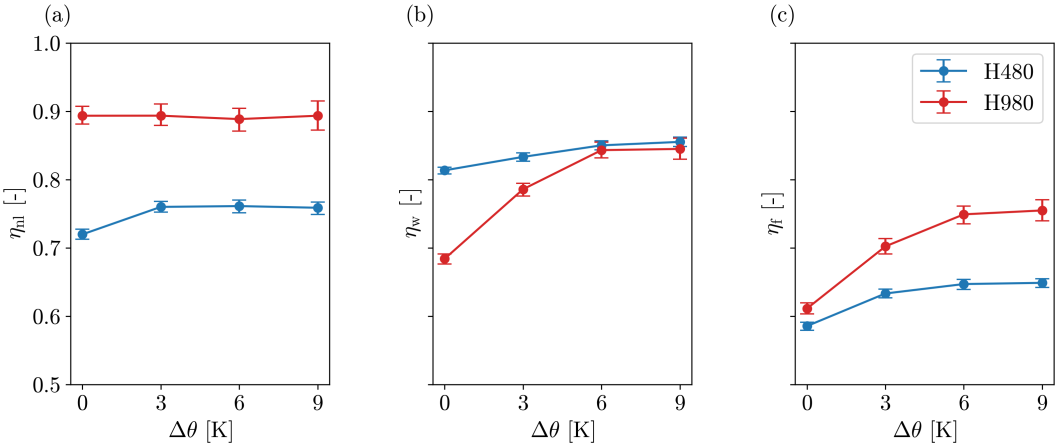

Figure 14. Non-local (a), wake (b) and farm (c) efficiencies computed from Eq. (6) as a function of the surface temperature difference $\Delta\theta$ for all the simulation cases. Error bars represent 95 % confidence intervals, obtained using moving block bootstrapping

320 isolated units in undisturbed free-stream flow (U_∞, a_∞). Secondly farm B, where all turbines experience free-stream velocity U_∞, but adopt the local axial induction a_{1n} of the actual front-row turbines inside the standard farm, which may be different from a_∞ because of pressure gradient and TI effects. Than farm C has every turbine behaving exactly like a front-row turbine

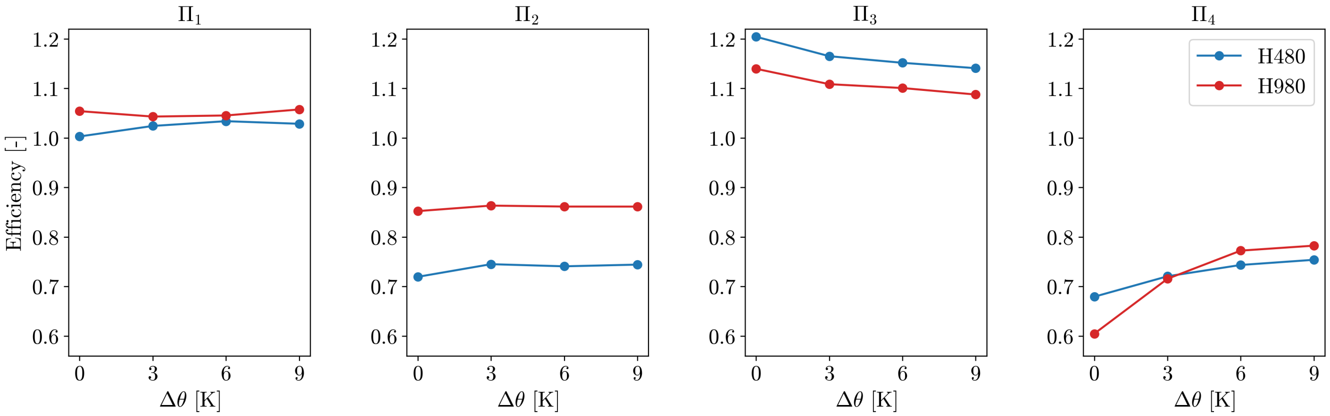

Figure 15. Efficiencies of the decomposition of η_f from Eq.(7) and (9).

inside the standard farm, incorporating the upstream flow slowdown ($U_{\mathrm{in},1n}, a_{1n}$). In farm D, Every turbine experiences the front-row inflow velocity $U_{\mathrm{in},1n}$ but maintains its own local axial induction a_{mn} from the standard farm. Lastly, the standard 325 farm E is the actual operating farm where each turbine mn experiences its true local inflow $U_{\mathrm{in},mn}$ and induction a_{mn}.

The power of a turbine at position mn is expressed as

$$P_{mn} = \frac{1}{2}\rho_0 A_d C_\mathrm{T}'(1-a_{mn})^3 U_{\mathrm{in},mn}^3. \quad (8)$$

Consequently, each efficiency Π_i is defined as the ratio between the total power of these successive farm states:

$$\begin{aligned}
\Pi_1 &= \frac{P_\mathrm{tot,B}}{P_\mathrm{tot,A}} = \frac{\sum_{n=1}^{N_\mathrm{t}^\mathrm{y}}(1-a_{1\mathrm{n}})^3}{N_\mathrm{t}^\mathrm{y}(1-a_\infty)^3},\\
\Pi_2 &= \frac{P_\mathrm{tot,C}}{P_\mathrm{tot,B}} = \frac{\sum_{n=1}^{N_\mathrm{t}^\mathrm{y}}(1-a_{1n})^3 U_{\mathrm{in},1n}^3}{\sum_{n=1}^{N_\mathrm{t}^\mathrm{y}}(1-a_{1n})^3 U_\infty^3},\\
\Pi_3 &= \frac{P_\mathrm{tot,D}}{P_\mathrm{tot,C}} = \frac{\sum_{m=1}^{N_\mathrm{t}^\mathrm{x}}\sum_{n=1}^{N_\mathrm{t}^\mathrm{y}}(1-a_{mn})^3}{N_\mathrm{t}^\mathrm{x}\sum_{\mathrm{n}=1}^{N_\mathrm{t}^\mathrm{y}}(1-a_{1n})^3} \quad \text{and}\\
\Pi_4 &= \frac{P_\mathrm{tot,E}}{P_\mathrm{tot,D}} = \frac{\sum_{m=1}^{N_\mathrm{t}^\mathrm{x}}\sum_{n=1}^{N_\mathrm{t}^\mathrm{y}}(1-a_{mn})^3 U_{\mathrm{in},mn}^3}{\sum_{m=1}^{N_\mathrm{t}^\mathrm{x}}\sum_{n=1}^{N_\mathrm{t}^\mathrm{y}}(1-a_{mn})^3 U_{\mathrm{in},1n}^3}.
\end{aligned} \quad (9)$$

330 Each ratio is constructed by varying either the local axial induction or the local inflow velocity while holding the other constant. This systematic isolation enables a decoupling of the underlying physical mechanisms: Π_1 and Π_3 capture the change in local axial induction possibly caused by the pressure gradients, whereas Π_2 and Π_4 identify the change on the local inflow velocity mostly attributed to improved vertical mixing and wake recovery.

The sensitivity of the decomposed efficiencies to the surface temperature jump ($\Delta\theta$) are presented in Fig. 15. The efficiency 335 Π_1 remains nearly constant across the range of $\Delta\theta$, with the front-row axial induction a_{1n} remaining slightly below the stand-alone value a_∞. As noted in Sec. 4.2 and Fig. 12a, this is likely a result of the favourable pressure gradient. Similarly, Π_2 remains unchanged but significantly below unity, reflecting a consistent flow slowdown upstream of the farm ($U_{\text{in},1n} < U_\infty$) caused by blockage-induced unfavourable pressure gradients. In contrast, Π_3 exhibits a slight decrease as $\Delta\theta$ increases, suggesting that the local axial induction throughout the farm (a_{mn}) converges toward the front-row values (a_{1n}). Despite this trend, Π_3 remains clearly above unity because a_{mn} is consistently smaller than a_{1n} (see Fig. 11c). This suggests that the favourable pressure gradient persists as a dominant driver even under strongly convective conditions ($\Delta\theta = 9$ K). The sensitivity to $\Delta\theta$ is most pronounced in Π_4, where the efficiency gain scales positively with the boundary layer height H. This trend suggests that higher $\Delta\theta$ values enable local inflow velocities $U_{\text{in},mn}$ to recover toward the front-row velocity $U_{\text{in},1n}$ more effectively. This behaviour is attributed to enhanced turbulent mixing in the convective boundary layer, which facilitates more rapid wake recovery. The substantial increase in Π_4 more than compensates for the marginal reduction in Π_3. Consequently, the net turbine efficiency η_w exhibits a positive correlation with $\Delta\theta$ across the investigated range. Overall, the analysis of the η_f components reveals that $\Delta\theta$ affects only the internal farm performance (Π_3, Π_4). Additionally, the unfavourable pressure gradient upstream of the farm and the favourable pressure gradient across the farm, remain impactful on the performance of the wind farm, even for strong convective conditions.

5 Conclusions

This study investigated the impact of hydrostatic blockage and gravity waves on the performance of large offshore wind farms operating within convective boundary layers (CBLs), a regime that has received limited attention compared to stable and neutral conditions. Using large-eddy simulations performed with the SP-Wind solver, we analysed the performance of a 1.5 GW offshore wind farm consisting of 100 IEA 15 MW turbines operating inside a CBL. Eight atmospheric scenarios, representative of cold-air outbreak situations, were explored by varying the capping-inversion height ($H = \{480, 980\}$ m) and the land–sea surface temperature difference ($\Delta\theta = \{0, 3, 6, 9\}$ K). These variations produced a diverse range of convective structures, including rolls, intermediate forms, and cells. The methodology involved first simulating a statistical steady-state conventional neutral boundary layer (CNBL) over land. The CBL was then obtained by transitioning the flow to a sea surface with reduced roughness and increased temperature. This transition period, characterized by significant changes in velocity, shear, and heat-flux profiles, was simulated for 1.5 h. Following this spin-up, a 1 h time-averaged analysis was performed on the wind farm performance and flow behavior.

The results demonstrate that a strong cold-air outbreak with a large surface temperature difference ($\Delta\theta$) leads to intensified convective mixing and a more rapid increase in the boundary layer height (H). This enhanced mixing results in increased buoyancy-driven turbulence, which promotes more effective wake recovery, generating a more uniform power distribution across the farm. Furthermore, the growth of the boundary layer slightly reduces both the unfavourable (Δp_u) and favourable (Δp_f) pressure gradients. However, this sensitivity is only observed for shallow boundary layers, where the relative increase in H is most pronounced. Efficiency analysis revealed that the wake efficiency (η_w) consistently increases with convective intensity, whereas non-local efficiency (η_nl) remains largely unaffected. Consequently, overall farm efficiency (η_f) improves under stronger convective forcing, though sensitivity diminishes at higher $\Delta\theta$. These trends were most pronounced for the deeper boundary layer cases ($H = 980$ m). Despite the increased convective mixing and the rising boundary layer height characteristic of the CBL, hydrostatic blockage and gravity waves persist in all cases. Even in the weakest blockage scenario ($H = 980$ m) $\eta_{\text{nl}} \approx 90\%$ was recorded. As the boundary layer height decreases, the impact of unfavourable and favourable pressure gradients on farm efficiency increases, while the influence of convective mixing diminishes.

These findings emphasize that mesoscale wave dynamics remain relevant even under buoyancy-dominated regimes and should be incorporated into wind farm design and performance modelling. While the present study focused on time-averaged quantities, future work could investigate time-dependent behaviour. Such analysis would clarify how specific convective structures such as rolls, cells, and intermediate forms influence turbine loading and power fluctuations, as well as how these distinct regimes affect overall wind farm performance.

Appendix A: Local turbine analysis

This study further investigates the local effects and performance of an individual turbine k within a wind farm. Characterizing these effects requires the definition of a local region extending both upstream and downstream, where the direct impact of the turbine on the flow field is dominant. The downstream region is categorized as the near-wake. Various methodologies exist to determine its spatial extent, L_{nw}. Notably, the downstream distance at which streamwise velocity deficit profiles transition to a Gaussian distribution (Dar et al., 2023) or the location where the wake deficit reaches its maximum value (Liew et al., 2024). Depending on the specific turbine operation (C'_{T}) and the state of the incoming flow (turbulence intensity and pressure gradients), L_{nw} typically ranges between $2D$ and $4D$ (Göçmen et al., 2016). The upstream region, or the turbine induction zone, is characterized by the length L_{ind}. For an isolated turbine, a common definition for L_{ind} is the upstream distance where the velocity is $98-99\%$ of the free-stream velocity. Correspondingly, the International Electrotechnical Commission (2005) standard recommends performing free-stream measurements at a distance $L_{\text{ind}} \geqslant 2-4D$ upstream. However, for waked turbines within a farm, the $98-99\%$ of the free-stream velocity thresholds are rarely reached locally, necessitating alternative definitions.

Three additional methods are evaluated based on averaging within a cylinder surrounding the turbine. In the first method, L_{ind} and L_{nw} are defined as the minimum distances where the streamwise gradient of the time-averaged velocity, U, falls below 2% of the gradient at the rotor disk, $\left|\frac{dU}{dx}\right| < 0.02\left|\frac{dU}{dx}\right|_{x=x_{\text{hub},mn}}$. In the second method, the lengths are determined where the streamwise gradient of the time-averaged pressure, p, is less than 2% of the gradient at the rotor disk, $\left|\frac{dp}{dx}\right| < 0.02\left|\frac{dp}{dx}\right|_{x=x_{\text{hub},mn}}$. For the last method, L_{ind} is equated to L_{nw}, with the latter defined by the location of the maximum wake deficit. Applying these methods to the LES data yields ranges of $L_{\text{ind}} = 1-3D$ and $L_{\text{nw}} = 1-2D$. The lengths L_{ind} and L_{nw} for the first two rows are consistently larger than those for the subsequent downstream rows (rows 3–10). This discrepancy stems primarily from the first two rows being non-waked and operating within the free-stream turbulence intensity (TI). In contrast, downstream rows are waked and subjected to higher TI, which leads to shorter characteristic induction lengths L (Revaz and Porté-Agel, 2025). Additionally, the favourable pressure gradient is less pronounced over the initial two rows, contributing to the larger

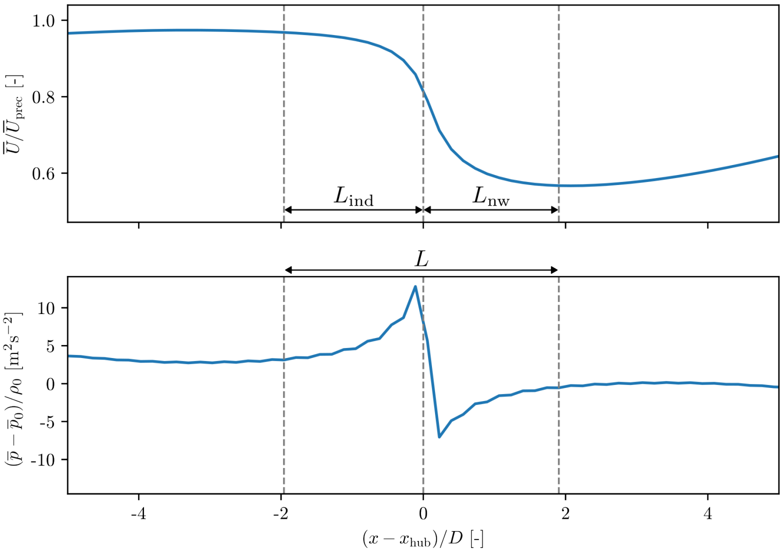

Figure A1. 1 h time-averaged (a) streamwise velocity and (b) pressure along a streamwise cylinder enveloping a turbine at the centre of the farm, and The vertical dashed lines denote the extent of the induction zone length L_{ind} and the near wake length L_{nw}.

L (Dar et al., 2023). Given that no single definition demonstrates clear superiority across all conditions, the method with $\left|\frac{dU}{dx}\right| < 0.02\left|\frac{dU}{dx}\right|_{x=x_{\mathrm{hub},mn}}$ is adopted. This approach also allows independent values of L_{ind} and L_{nw}. The characteristic local length is than defined as $L = L_{\mathrm{ind}} + L_{\mathrm{nw}}$.

405 Figure A1 shows L_{ind}, L_{nw} and L for turbine $k = 45$, located in the centre of the farm, for case H980–$\Delta\theta 0$. Based on this region, we can define the local axial induction of turbine k as,

$$a_{mn} = 1 - \frac{U_{\mathrm{d},mn}}{U_{\mathrm{in},mn}}, \tag{A1}$$

where $U_{\mathrm{d,mn}}$ is the streamwise velocity averaged over the rotor disk and $U_{\mathrm{in},mn} = U_{mn}(x = -L_{\mathrm{ind}})$ is the local inflow velocity of turbine mn. Additionally we define the local pressure drop across turbine mn as,

410 $$\Delta p_{mn} = p_{mn}(x = L_{\mathrm{nw}}) - p_{mn}(x = -L_{\mathrm{ind}}), \tag{A2}$$

where $p_{mn}(x)$ is the 1 h time-averaged pressure perturbation, averaged along a streamwise cylinder enveloping the turbine at position mn.

Code availability. The Navier–Stokes solver used in this work is SP-Wind, a proprietary software with restricted access. Access may be granted upon reasonable request.

Data availability. The full dataset generated during the study is available from the corresponding author upon reasonable request. The data and the Python scripts necessary to reproduce the figures in this study are openly available as a KU Leuven RDR dataset:

Author contributions. ON and JM jointly defined the methodology and set up the simulation studies in the current work. ON carried out the simulations and post-processing. ON and JM wrote the manuscript.

Competing interests. At least one of the (co-)authors is a member of the editorial board of Wind Energy Science. The authors have no other competing interests to declare.

Acknowledgements. The computational resources and services used in this work were provided by the VSC (Flemish Supercomputer Center), funded by the Research Foundation - Flanders (FWO) and the Flemish Government.

Financial support. Project Cloud4Wake, funded by Vlaamse Agentschap Innoveren & Ondernemen (VLAIO) under Blue Cluster cSBO programme (Contract number HBC.2022.0549)

References

Allaerts, D. and Meyers, J.: Boundary-layer development and gravity waves in conventionally neutral wind farms, Journal of Fluid Mechanics, 814, 95–130, https://doi.org/10.1017/jfm.2017.11, 2017.

Allaerts, D. and Meyers, J.: Gravity Waves and Wind-Farm Efficiency in Neutral and Stable Conditions, Boundary-Layer Meteorology, 166, 269–299, https://doi.org/10.1007/s10546-017-0307-5, 2018.

Atkinson, B. W. and Wu Zhang, J.: Mesoscale shallow convection in the atmosphere, Reviews of Geophysics, 34, 403–431, https://doi.org/https://doi.org/10.1029/96RG02623, 1996.

Bleeg, J.: A numerical study of the influence of terrain on wakes, blockage, wind farm efficiency, and turbine efficiency, Wind Energy Science Discussions, https://doi.org/10.5194/wes-2025-291, preprint in review, 2026.

Calaf, M., Meneveau, C., and Meyers, J.: Large eddy simulation study of fully developed wind-turbine array boundary layers, Physics of Fluids, 22, 015 110, https://doi.org/10.1063/1.3291077, 2010.

Dar, A. S., Gertler, A. S., and Porté-Agel, F.: An Experimental and Analytical Study of Wind Turbine Wakes under Pressure Gradient, 35, 045 140, https://doi.org/10.1063/5.0145043, 2023.

Deardorff, J. W.: Numerical Investigation of Neutral and Unstable Planetary Boundary Layers, Journal of Atmospheric Sciences, 29, 91 – 115, https://doi.org/10.1175/1520-0469(1972)029<0091:NIONAU>2.0.CO;2, 1972.

Deardorff, J. W.: Stratocumulus-capped mixed layers derived from a three-dimensional model, Boundary-Layer Meteorology, 18, 495–527, https://doi.org/10.1007/BF00119502, 1980.

Delvaux, T. and Meyers, J.: A large-eddy simulation analysis of collective wind farm axial-induction set points in the presence of blockage, Wind Energy Science, 10, 613–630, https://doi.org/10.5194/wes-10-613-2025, 2025.

Gaertner, E., Abbas, N., Barter, G., et al.: IEAWindSystems/IEA-15-240-RWT: Release v1.1.0, https://doi.org/10.5281/zenodo.3951793, 2020a.

Gaertner, E., Rinker, J., Sethuraman, L., et al.: Definition of the IEA 15-Megawatt Offshore Reference Wind Turbine, Tech. Rep. NREL/TP-5000-75698, National Renewable Energy Laboratory, Golden, CO, https://www.nrel.gov/docs/fy20osti/75698.pdf, 2020b.

Göçmen, T., Laan, P. V. D., Réthoré, P.-E., Diaz, A. P., Larsen, G. C., and Ott, S.: Wind Turbine Wake Models Developed at the Technical University of Denmark: A Review, Renewable and Sustainable Energy Reviews, 60, 752–769, https://doi.org/10.1016/j.rser.2016.01.113, 2016.

Goit, J. and Meyers, J.: Optimal control of energy extraction in wind-farm boundary layers, Journal of Fluid Mechanics, 768, 5–50, https://doi.org/10.1017/jfm.2015.70, 2015.

International Electrotechnical Commission: Wind turbines, Part 12-1: Power performance measurements of electricity producing wind turbines, Tech. Rep. IEC 61400-12-1, International Electrotechnical Commission, https://webstore.iec.ch/publication/68499, accessed: 8 July 2024, 2005.

Jamaer, S., Allaerts, D., Meyers, J., and Lipzig, N. P. V.: A Novel Framework for Spatiotemporal Analysis of Temperature Profiles Applied to Europe, Journal of Applied Meteorology and Climatology, 62, 1855–1873, https://doi.org/10.1175/JAMC-D-22-0205.1, 2023.

Lanzilao, L. and Meyers, J.: An Improved Fringe-Region Technique for the Representation of Gravity Waves in Large Eddy Simulation with Application to Wind Farms, 2023.

Lanzilao, L. and Meyers, J.: A parametric large-eddy simulation study of wind-farm blockage and gravity waves in conventionally neutral boundary layers, Journal of Fluid Mechanics, 979, A54, https://doi.org/10.1017/jfm.2023.1088, 2024.

Liew, J., Heck, K. S., and Howland, M. F.: Unified Momentum Model for Rotor Aerodynamics across Operating Regimes, Nature Communications, 15, 6658, https://doi.org/10.1038/s41467-024-50756-5, 2024.

Lignarolo, L. E., Mehta, D., Stevens, R. J., Yilmaz, A. E., van Kuik, G., Andersen, S. J., Meneveau, C., Ferreira, C. J., Ragni, D., Meyers, J., van Bussel, G. J., and Holierhoek, J.: Validation of four LES and a vortex model against stereo-PIV measurements in the near wake of an actuator disc and a wind turbine, Renewable Energy, 94, 510–523, 2016.

Lu, H. and Porté-Agel, F.: On the Impact of Wind Farms on a Convective Atmospheric Boundary Layer, Boundary-Layer Meteorology, 157, 81–96, https://doi.org/10.1007/s10546-015-0049-1, 2015.

Maas, O.: Large-eddy simulation of a 15 GW wind farm: Flow effects, energy budgets and comparison with wake models, Frontiers in Mechanical Engineering, Volume 9 - 2023, https://doi.org/10.3389/fmech.2023.1108180, 2023a.

Maas, O.: From gigawatt to multi-gigawatt wind farms: wake effects, energy budgets and inertial gravity waves investigated by large-eddy simulations, Wind Energy Science, 8, 535–556, https://doi.org/10.5194/wes-8-535-2023, 2023b.

Maas, O. and Raasch, S.: Wake properties and power output of very large wind farms for different meteorological conditions and turbine spacings: A large-eddy simulation case study for the German Bight, Wind Energy Science, 7, 715–739, https://doi.org/10.5194/wes-7-715-2022, 2022.

Martínez-Tossas, L. A., Churchfield, M. J., Yilmaz, A. E., Sarlak, H., Johnson, P. L., Sørensen, J. N., Meyers, J., and Meneveau, C.: Comparison of four large-eddy simulation research codes and effects of model coefficient and inflow turbulence in actuator-line-based wind turbine modeling, Journal of Renewable and Sustainable Energy, 10, 033 301, 2018.

Meyers, J. and Meneveau, C.: Large Eddy Simulations of Large Wind-Turbine Arrays in the Atmospheric Boundary Layer, ISBN 978-1-60086-959-4, https://doi.org/10.2514/6.2010-827, 2010.

Müller, G. and Chlond, A.: Three-Dimensional Numerical Study of Cell Broadening during Cold-Air Outbreaks, Boundary-Layer Meteorology, 81, 289–323, https://doi.org/10.1007/BF02430333, 1996.

Munters, W., Meneveau, C., and Meyers, J.: Turbulent Inflow Precursor Method with Time-Varying Direction for Large-Eddy Simulations and Applications to Wind Farms, Boundary-Layer Meteorology, 159, https://doi.org/10.1007/s10546-016-0127-z, 2016.

Nappo, C. J.: Wave Stress, https://doi.org/https://doi.org/10.1016/B978-0-12-385223-6.00006-9, 2012.

Ndindayino, O., Puel, A., and Meyers, J.: Effect of Blockage on Wind Turbine Power and Wake Development, Wind Energy Science, 10, 2079–2098, https://doi.org/10.5194/wes-10-2079-2025, 2025.

Rampanelli, G. and Zardi, D.: A Method to Determine the Capping Inversion of the Convective Boundary Layer, Journal of Applied Meteorology - J APPL METEOROL, 43, 925–933, https://doi.org/10.1175/1520-0450(2004)043<0925:AMTDTC>2.0.CO;2, 2004.

Revaz, T. and Porté-Agel, F.: Effect of Turbulence Intensity on the Induction Factor and Power Efficiency of Wind Turbines, 28, e70 040, https://doi.org/10.1002/we.70040, 2025.

Salesky, S., Chamecki, M., and Bou-Zeid, E.: On the Nature of the Transition Between Roll and Cellular Organization in the Convective Boundary Layer, Boundary-Layer Meteorology, 163, https://doi.org/10.1007/s10546-016-0220-3, 2017.

Sanchez Gomez, M., Lundquist, J., Mirocha, J., and Arthur, R.: Investigating the Physical Mechanisms that Modify Wind Plant Blockage in Stable Boundary Layers, Wind Energy Science, 8, 1049–1069, https://doi.org/10.5194/wes-8-1049-2023, 2023.

Shapiro, C. R., Gayme, D. F., and Meneveau, C.: Filtered actuator disks: Theory and application to wind turbine models in large eddy simulation, Wind Energy, 22, 1414–1420, https://doi.org/https://doi.org/10.1002/we.2376, 2019.

Sood, I., Simon, E., Vitsas, A., Blockmans, B., Larsen, G. C., and Meyers, J.: Comparison of large eddy simulations against measurements from the Lillgrund offshore wind farm, Wind Energy Science, 7, 2469–2489, https://doi.org/10.5194/wes-7-2469-2022, 2022.

https://doi.org/10.5194/wes-2026-49
Preprint. Discussion started: 31 March 2026

Souaiby, M. and Porté-Agel, F.: Atmospheric stability effect on wind farm flow and performance, Physics of Fluids, 37, 095 152, https://doi.org/10.1063/5.0280027, 2025.

Stipa, S., Ajay, A., Allaerts, D., and Brinkerhoff, J.: TOSCA – an open-source, finite-volume, large-eddy simulation (LES) environment for wind farm flows, Wind Energy Science, 9, 297–320, https://doi.org/10.5194/wes-9-297-2024, 2024.

Verstappen, R. and Veldman, A.: Symmetry-preserving discretization of turbulent flow, Journal of Computational Physics, 187, 343–368, https://doi.org/10.1016/S0021-9991(03)00126-8, 2003.

Wen, Z., Markfort, C. D., and Porté-Agel, F.: Wind-Turbine Wakes in a Convective Boundary Layer: A Wind-Tunnel Study, Boundary-Layer Meteorology, 146, 161–179, https://doi.org/10.1007/s10546-012-9751-4, 2013.

Wulfmeyer, V., Muppa, S. K., Behrendt, A., Hammann, E., Späth, F., Sorbjan, Z., Turner, D. D., and Hardesty, R. M.: Determination of Convective Boundary Layer Entrainment Fluxes, Dissipation Rates, and the Molecular Destruction of Variances: Theoretical Description and a Strategy for Its Confirmation with a Novel Lidar System Synergy, Journal of the Atmospheric Sciences, 73, 667 – 692, https://doi.org/10.1175/JAS-D-14-0392.1, 2016.